Charge Storage Mechanism of Nanostructured Anhydrous and Hydrous Ruthenium-Based Oxides

Wataru Sugimoto,[1,*] Katsunori Yokoshima, Yasushi Murakami, and Yoshio Takasu[1]

Department of Fine Materials Engineering, Faculty of Textile Science and Technology, Shinshu University, 3-15-1 Tokida, Ueda 386-8567, JAPAN

Abstract

The charge storage mechanism of nanostructured anhydrous and hydrous ruthenium-based oxides was evaluated by various electrochemical techniques (cyclic voltammety, hydrodynamic voltammetry, chronoamperometry, and electrochemical impedance spectroscopy). The effects of various factors, such as particle size, hydrous state, and structure, on the pseudocapacitive property were characterized. The electric double layer capacitance (C_{dl}), adsorption related charge (C_{ad}), and the irreversible redox related charge (C_{irr}) per unit mass and surface area of electrode material has been estimated and the role of structural water within the material either in micropores or interlayer are discussed.

Keywords: Electrochemical supercapacitors; Ruthenium oxide; Electric double layer; Pseudocapacitance

* Corresponding author. Tel.: +81-268-21-5455; Fax: +81-268-21-5452

E-mail address: wsugi@shinshu-u.ac.jp (W. Sugimoto).
[1] ISE member

1. Introduction

Electrochemical capacitors (also known as supercapacitors or ultracapacitors) are attractive devices characterized by high power, high energy density with long cycle life [1-5]. In particular, electrochemical capacitors employing ruthenium oxide as electrode material (so-called pseudo-capacitors or redox-capacitors due to their surface redox activity compared to their carbon analog) are capable of providing high gravimetric and volumetric energy density [1,5-11]. Thus, RuO_2-based supercapacitors are potential candidates as power sources for small devices.

RuO_2-based materials have been extensively studied as electrode materials in particular for various gas evolution electrodes (chlorine, oxygen, and hydrogen) [12-15]. Since the pioneering study by Trasatti and Buzzanca [16] who first recognized that the 'rectangular' shaped cyclic voltammogram of a RuO_2 film resembled that of the electric double layer capacitors, much effort has been devoted to enhancing the capacitance as well as the fundamental understanding of the mechanism of the pseudocapacitance. Despite the extensive amount of these and other studies, the fundamental charge storage properties of RuO_2, for example the contribution of redox capacitance, is still not well understood and a universal understanding on the redox properties towards supercapacitor application has yet to be established. The fast and slow charges in thermally prepared DSA-type electrodes have been attributed to the utilization of more accessible, mesoporous surfaces and less accessible, microporous inner-surfaces, respectively [17]. Based on ellipsometry and ac impedance measurements on anodically and thermally prepared RuO_2, the fast- and slow-charging modes have been attributed to

the charging of the grain surfaces and incorporation of protons into the oxide grains, respectively [18].

The study on hydrous ruthenium oxide ($RuO_2 \cdot xH_2O$) prepared by a sol-gel procedure constituted to a major advance in terms of gravimetric capacitance [19,20]. The specific capacitance for hydrous ruthenium oxide ($RuO_2 \cdot xH_2O$) ranges from 600 to 1,000 F g^{-1} depending on the preparation procedure, measurement conditions, use of support, etc [19-35]. Another type of hydrous ruthenium oxide, layered ruthenic acid hydrate ($H_{0.2}RuO_{2.1} \cdot nH_2O$), is also a promising electrode material with mixed protonic-electronic conduction [10,36-39]. Unlike $RuO_2 \cdot xH_2O$, layered $H_{0.2}RuO_{2.1} \cdot nH_2O$ is a lamellar crystalline oxide, and the electronic conduction is provided via 0.4 nm thick crystalline ruthenium oxide slabs that are interleaved in a nanometer scale with a hydrous layer accounting for the protonic conduction. Specific capacitance up to 400 F g^{-1} can be achieved with this material. Furthermore, specific capacitance up to 660 F g^{-1}, which is comparable with $RuO_2 \cdot xH_2O$, can be achieved by utilizing ruthenium oxide nanosheets derived from $H_{0.2}RuO_{2.1} \cdot nH_2O$ by chemical exfoliation (de-lamination). The discovery of these new hydrated materials as a supercapacitor material has brought about a new topic to be considered in the electrochemical charge storage mechanism, namely the effect of water in the electrode material.

The impact of structural water on the capacitive properties is not well documented and seems to be controversial. Although $RuO_2 \cdot xH_2O$ can deliver higher energy density compared to anhydrous RuO_2, such high energy density generally cannot be obtained at

high current density. Various explanations have been proposed so far to explain the increase in energy density and corresponding decrease in power density with increasing water content in $RuO_2 \cdot xH_2O$. It has been proposed that the hydrous regions within the nanoparticles allows facile proton permeation into the bulk material for efficient charge storage while the interconnected ruthenium oxide region accounts for the electronic conduction [20]. The specific capacitance is also known to strongly correlate with the proton mobility [24]. An optimum mixed percolation conduction mechanism where separate percolation paths provide protonic and electronic conduction has also been proposed [31].

This paper will focus on the charge storage mechanism of ruthenium-based oxides evaluated by various electrochemical methods using anhydrous and hydrous ruthenates with a variety of structures and composition. Various materials will be compared. Namely, anhydrous RuO_2 deposited on a flat glassy carbon surface (model electrode) and thin films of anhydrous RuO_2 nanoparticles, hydrous ruthenium oxide, layered ruthenic acid, and ruthenic acid nanosheets.

2. Experimental

The preparation and structural characterization of RuO_2 model electrodes [40], anhydrous RuO_2 nanoparticles [41,42], hydrous RuO_2 nanoparticles ($RuO_2 \cdot 0.5H_2O$) [38,39], layered ruthenic acid hydrate ($H_{0.2}RuO_{2.1} \cdot nH_2O$) [36,37], and ruthenium oxide nanosheets, ($(RuO_{2.1-\alpha}(OH)_\alpha)^{\alpha-}{}_\infty$) [36], were reported in detail earlier. Electrochemical measurements were conducted with a beaker-type electrochemical cell at 25°C. The cell

was equipped with a working electrode, a platinum mesh counter electrode, and an Ag/AgCl reference electrode. Electrode potentials will be referred to the reversible hydrogen electrode (RHE) potential scale throughout this paper. A Luggin capillary faced the working electrode at a distance of 2 mm.

The working electrodes for the model electrodes were prepared by dropping solutions of $RuCl_3$ dissolved in butyl alcohol onto buff-polished glassy carbon electrodes. The electrodes were heat treated at 400°C in air to convert the precursor to RuO_2. These RuO_2 modified glassy carbon model electrodes were used as working electrodes without further treatment. The working electrodes for anhydrous RuO_2, $RuO_2{\cdot}0.5H_2O$, $H_{0.2}RuO_{2.1}{\cdot}nH_2O$ thin films was composed of 40 μg of active material stabilized on a glassy carbon surface with a thin layer of re-cast Nafion ionomer. Re-stacked nanosheet electrodes were prepared by dropping 20 μL of a colloidal suspension (3.6 mg of RuO_2 per 20 mL in distilled water) onto a mirror-polished glassy carbon rod. The capacitance was calculated by averaging the anodic and cathodic charge.

3. Results and discussion

3.1. Particle size effects of anhydrous RuO_2 nanoparticles

The so-called “model electrode method”, where a known amount of active material is dispersed on the surface of a microscopically flat glassy carbon rod surface, is a powerful and reliable method to study the size effects of supported metal particles, since the influence caused by the porosity in the supporting materials can be eliminated [43].

This method was employed for the characterization of the particle size effect towards supercapacitor behavior of anhydrous RuO_2 nanoparticles.

Figure 1 shows the increase in the gravimetric capacitance with decreasing amount of RuO_2 loaded on the glassy carbon surface. A simple calculation of the trend in the surface area and gravimetric capacitance as a function of the particle size is shown in Fig. 2. The gravimetric capacitance was estimated using the value of C = 80 μF cm^{-2} [41,44,45] as a probe. At a particle size of ~0.9 nm, the estimated capacitance is ~760 F g^{-1}. This value is comparable to the gravimetric capacitance of $RuO_2 \cdot xH_2O$, clearly indicating that the particle size has a significant impact on the total capacitance.

-----Figure 1-----

-----Figure 2-----

3.2. Evaluation of the redox capacitance of anhydrous RuO_2 nanoparticles

A slightly more complex system than the model electrode, a thin film electrode, was employed to elucidate the redox behavior of structurally well-characterized nanoparticulate RuO_2. This method allows the straightforward evaluation of nanoparticulate RuO_2 with a known amount of electrode mass and surface area at a wide range of scan rates, which in turn allows quantitative evaluation of the specific capacitance. The active material was mesoporous anhydrous RuO_2 (average particle size=10 nm, S_{BET}= 42 m^2 g^{-1}, average pore diameter=16 nm, 90% mesoporosity).

Figure 3 shows the cyclic voltammograms of anhydrous RuO_2 at slow to fast scan rates (0.5-500 mV s^{-1}). From the scan rate independent cathodic region (1.3 to 1.1 V),

the electric double layer capacitance of RuO_2 can be calculated as C_{dl}=34 F g^{-1}, or 80 μF cm^{-2}. A large, strongly scan rate dependent cathodic current is observed at potentials below 0.4 V. Small but detectable, weakly scan rate dependent redox peaks at E~0.6 and 0.8 V are also observed.

The discharge of the cathodic charge at $E \leq 0.4$ V is completely regained on the anodic scan although it is spread over the whole anodic range. The possibility of hydrogen evolution can be excluded, since such a reaction would lead to a difference between the cathodic and anodic charges. Hydrogen absorption, which can only occur at potentials just above the hydrogen evolution region [46], can also be disregarded. The large cathodic current below 0.4 V can thus be attributed to charge storage within the grain boundaries (grain-boundary charging). The contribution of this charge to the total capacitance can be evaluated by simply subtracting the capacitance measured at two different potential windows, $C_{0.1–1.3} - C_{0.4–1.3}$. A linear relation was obtained by plotting $C_{0.1–1.3} - C_{0.4–1.3}$ versus $v^{-1/2}$, which indicates that this charge is diffusion limited and originates from an electrochemically irreversible Faradaic reaction (C_{irr}). The contribution from C_{irr} at 500 mV s^{-1} was C_{irr}~2 F g^{-1} or 5% of the overall capacitance (C_{all}), and increased with decreasing scan rates to C_{irr}=32 F g^{-1}, or 40% of C_{all} at 0.5 mV s^{-1}.

The two small redox peaks at 0.6 and 0.8 V are attributed to electrosorption of ionic species on the surface of RuO_2 (C_{ad}). This charge storage is faster than C_{irr}, although not as fast as the C_{dl}. Hydrodynamic voltammetry at a disk rotation of 3600 rpm revealed that the redox peak at ~0.8 V is less dependent on the electrode rotation compared to

that of the 0.6 V peak. Moreover, these peaks were not evident in KOH electrolyte. The results suggest that the redox peaks at 0.6 and 0.8 V can be attributed to electrosorption of anions and cations, respectively. This is in accordance with previous in-situ EQCM studies of electrolytic RuO_2 revealing mass gain and loss near these two redox peaks [33]. The contribution of C_{ad} at 0.5 mV s^{-1} is estimated as C_{ad}~17 F g^{-1} (42 μF cm^{-2}) using the values of C_{dl}~34 F g^{-1} (80 μF cm^{-2}) and C_{irr}~31 F g^{-1} (75 μF cm^{-2}). This C_{ad} value corresponds to a surface reaction of approximately 0.2 electrons per surface RuOH.

The pseudocapacitance of anhydrous RuO_2 nanoparticles can thus be deconvoluted into at least 3 major components (C_{dl}, C_{irr}, C_{ad}) with different kinetics within the potential range of 0.1–1.3 V. Figure 4 illustrates the change in specific capacitance as a function of the scan rate.

-----Figure 4-----

3.3. Charge storage mechanism of hydrous RuO_2 nanoparticles

Cyclic voltammograms at various scan rates for $RuO_2 \cdot 0.5H_2O$ are shown in Fig. 5. Compared to anhydrous RuO_2, C_{ad} at 0.6 and 0.8 V and C_{irr} below 0.4 V are not evident, leading to featureless and rectangular shaped voltammograms. The lack of C_{irr} below 0.4 V for the hydrated system can be attributed to the fact that there is no grain-boundary charging since most or all grain boundaries are hydrated.

-----Figure 5-----

The impedance data for anhydrous RuO_2 and $RuO_2 \cdot 0.5H_2O$ at various potentials are

compared in Fig. 6. The frequency where ϕ=-45° ($f_{\phi=-45}$) can be recognized as the frequency response to the ideally capacitive behavior for a single electrode (capacitor response frequency). The capacitor response frequency (shown with left arrows in the figures) was $f_{\phi=-45}$=2-4 Hz for $RuO_2 \cdot 0.5H_2O$, which is considerably lower than that observed for anhydrous RuO_2 ($f_{\phi=-45}$=50-130 Hz), giving the response time of the capacitor (single electrode) at 500-250 ms (20-10 ms for anhydrous RuO_2). The knee frequency characterizes the lower limit of the high frequency region, thus the frequency distinguishing the transition from the high frequency to the medium frequency region. The knee frequencies (shown with bottom arrows in the figures) for $RuO_2 \cdot 0.5H_2O$ are in the same range as anhydrous RuO_2, indicating that the charge-transfer resistance is independent of the water content. The change in the electronic conductivity can thus be considered as an insignificant contribution to the capacitor frequency response. The capacitor response frequency and characteristic knee frequency are listed in Table 1.

-----Figure 6-----

The impedance data can be fitted assuming three major reactions at high, medium, and low frequency. A model circuit (Fig. 6 inset) comprised of 7 elements was adopted to fit the impedance data. Here R_s is the solution resistance, C is the capacitance at high frequency of the outer most surface of the film, and Z_W is the finite length Warburg impedance element. A CPE element was used to account for the low frequency Faradaic

impedance considering the inhomogeneity of the film. The fitted data agrees well with the experimental data throughout the whole frequency range studied.

At high frequency ($f \geq 2.5$ kHz), the impedance is dominated by the charge transfer process at the outer most surface of the electrode in contact with the electrolyte. The medium frequency region is diffusion controlled, and the distributed capacitance and resistance within the film will dominate the impedance. At the low frequency range ($f \leq f_{\phi=-45}$), non-homogeneous diffusion in the less-accessible sites should govern the impedance. Selected parameters extracted from fitting the impedance data to the equivalent circuit (shown in inset of Fig. 6) are listed in Table 1.

The Warburg parameter T_W was significantly larger for $RuO_2 \cdot 0.5H_2O$ than anhydrous RuO_2. The larger T_W value is interpreted as a result of the increase in the effective thickness L due to the utilization of less-accessible active sites, such as micropores. The less accessible micropores should suffer from diffusion limitations, and the apparent increase in the effective thickness can be interpreted as the increase in the utilization of hydrated micropores. Mesopores are less influenced by diffusion limitations, giving the high capacitor frequency response with the sacrifice of specific capacitance.

The above scheme can be visualized as high conducting ‘freeways’ for fast charging and low conducting ‘city roads’ for slow charging. The freeways are the mesopores

constituted from secondary particles, where the effect of mass transfer is less significant. On the other hand, charging of the micropores is mass transfer controlled since the ionic resistance is high. The capacitance in $RuO_2 \cdot 0.5H_2O$ originates from both the easily accessible mesopores (freeways), and the less accessible micropores (city roads). The utilization of micropores (city roads) results in high specific capacitance but gives low capacitor frequency response. On the other hand, the majority of the capacitance in anhydrous RuO_2 originates from the easily accessible mesopores (highway) with almost no contribution from micropores (city roads). Thereby, the capacitor frequency response is high but the specific capacitance is low because of the low surface utilization. The larger value of the effective thickness *L* for the hydrated systems can thus be taken as the development of city roads.

3.4. Charge storage mechanism of layered $H_{0.2}RuO_{2.1} \cdot nH_2O$ and its nanosheet derivative

Layered $H_{0.2}RuO_{2.1} \cdot nH_2O$ is a lamellar oxide composed of 0.4 nm crystalline ruthenium oxide slabs interleaved with a hydrous interlayer. It possesses metallic conductivity with room-temperature resistivity in the order of mΩ cm [37] and ionic conductivity via the hydrous interlayer. The Ru oxidation state is predominantly 4+, which makes this compound extremely electrochemically stable. The water content *n* is typically $n \sim 0.9$ for a room-temperature dried product and tri- and di-hydrated phases can be obtained depending on the conditions. Chemical modification of layered

$H_{0.2}RuO_{2.1}{\cdot}nH_2O$ can be conducted to exfoliate the ruthenium oxide slabs into colloidal nanosheets.

The cyclic voltammograms of layered $H_{0.2}RuO_{2.1}{\cdot}nH_2O$ and re-stacked nanosheets (Fig. 7) have a mirror image with well-defined redox peaks centered at 0.6 and 0.9 V. Such peaks are evident in anhydrous RuO_2, although not as profound [41]. These peaks are sensitive to the electrolyte, indicating the involvement of ion electrosorption. The 0.6 and 0.9 V peaks are attributed to electrosorption of cationic and ionic species (C_{ad}). The larger contribution from these redox-related charges is attributed to the advantageous ionic transport through the expandable hydrous interlayer.

-----Figure 7-----

The C_{dl} calculated from the rectangular-shape 'background' current is ~200 F g^{-1} for both layered $H_{0.2}RuO_{2.1}{\cdot}nH_2O$ and re-stacked nanosheets. This is roughly a 6 times increase compared to anhydrous RuO_2 nanoparticles. Using the value of ~80 μF cm^{-2} as a probe, a specific surface area of 250 m^2 g^{-1} is derived, which is considerably larger than the surface area measured from N_2 adsorption/desorption studies of 57 m^2 g^{-1}. The extremely high electrochemically active surface area can only be explained by assuming that the interlayer surface of $H_{0.2}RuO_{2.1}{\cdot}nH_2O$ is active for double layer charging. Due to the high electrochemically active surface area and large contribution from C_{ad}, specific capacitance of 400 F g^{-1} can be achieved with $H_{0.2}RuO_{2.1}{\cdot}nH_2O$ and 660 F g^{-1} for re-stacked nanosheets. The higher capacitance for re-stacked nanosheets can be easily interpreted as the higher utilization of C_{ad} because of the open structure allowing facile ion diffusion into the interlayer space.

The impedance behavior of layered $H_{0.2}RuO_{2.1}\cdot nH_2O$ is similar to $RuO_2\cdot 0.5H_2O$. The capacitor response frequency $f_{\phi=-45}$ ranged from 2-5 Hz, giving the response time of the capacitor at 500-200 ms, similar to the values for $RuO_2\cdot 0.5H_2O$. The knee frequency for layered $H_{0.2}RuO_{2.1}\cdot nH_2O$ is observed at 0.3-0.6 kHz. In the case of layered $H_{0.2}RuO_{2.1}\cdot nH_2O$, the easily accessible mesopores (highway) are constructed from the interparticle mesoporous voids. The less accessible region (city roads) originates from the expandable hydrous interlayer.

4. Conclusions

The electrochemical capacitor behavior of anhydrous RuO_2 model electrode, and anhydrous RuO_2, hydrous RuO_2, layered $H_{0.2}RuO_{2.1}\cdot nH_2O$, ruthenic acid nanosheets thin films were evaluated and the charge storage mechanism was discussed. The overall capacitance in ruthenium-based oxides can be deconvoluted into three major contributions. Namely, the electric double layer capacitance (C_{dl}), adsorption related charge (C_{ad}), and the irreversible redox related charge (C_{irr}). C_{ad} is strongly dependent on the structure of material. Layered $H_{0.2}RuO_{2.1}\cdot nH_2O$ and ruthenic acid nanosheets exhibit large C_{ad}, whereas it is not as obvious in $RuO_2\cdot 0.5H_2O$. C_{irr} was not observed in hydrous materials such as $RuO_2\cdot 0.5H_2O$ and layered $H_{0.2}RuO_{2.1}\cdot nH_2O$, which has been attributed to the lack of grain-boundary charging. In general, the smaller the particle size, higher gravimetric capacitance can be obtained due to the increase in surface area. The hydrous state is a key factor in terms of both energy and power density. Ionic conduction via hydrous micropores, mesopores, or interlayer most likely dominates the

capacitive behavior.

Acknowledgements

This work was supported in part by an Industrial Technology Research Grant Program (02B63013c) from the New Energy and Industrial Technology Development Organization (NEDO) and Grants-in-Aid for Scientific Research (16750170, 17350097) a 21st Century COE Program from Ministry of Education, Science, Sports, and Culture (MEXT).

References

1. B.E. Conway, Electrochemical Supercapacitors, Kluwer Academic Pub., Norwell, MA, 1999.
2. I.E. Raistrick, in: J. McHardy, F. Ludwig (Eds), Electrochemistry of Semiconductors and Electronics, Noyes Publications, Park Ridge, NJ, 1992, p. 297.
3. A. Nishino, J. Power Sources 60 (1996) 137.
4. E. Faggioli, P. Rena, V. Danel, X. Andriu, R. Mallant, H. Kahlen, J. Power Sources 84 (1999) 261.
5. A. Burke, J. Power Sources 91 (2000) 37.
6. B. E. Conway, J. Electrochem. Soc. 138 (1991) 1539.
7. S. Trasatti, Electrochim. Acta 36 (1991) 225.
8. S. Sarangapani, B. V. Tilak, C.-P. Chen, J. Electrochem. Soc. 143 (1996) 3791.
9. B.E. Conway, V. Birss, J. Wojtowicz, J. Power Sources 66 (1997) 1.
10. Y. Takasu, Y. Murakami, Electrochim. Acta 45 (2000) 4135.
11. C. Angelinetta, S. Trasatti, L. D. Atanasoska, R. T. Atanasoski, J. Electroanal. Chem. 214 (1986) 535.
12. S. Trasatti, G. Lodi, in: S. Trasatti (Ed.), Electrodes of Conducting Metallic Oxides, part B, Ed. , Elsevier, Amsterdam, 1981, Ch.10.
13. S. Trasatti, in: H. Gerischer, C.W. Tobias (Ed.), Advances in Electrochemical Science and Engineering, vol. 2, VCH, Weinheim, 1992, Ch. 1.
14. S. Trasatti, Electrochim. Acta 45 (2000) 2377.
15. S. Trasatti, Electrochim. Acta 32 (1987) 369.
16. S. Trasatti, G. Buzzanca J. Electroanal. Chem. 29 (1971) App 1.
17. Aridizzone, G. Fregonara, S. Trasatti, Electrochim. Acta 35 (1990) 263.
18. Rishpon, S. Gottesfeld, J. Electrochem. Soc. 131 (1984) 1960.
19. J.P. Zheng, T.R. Jow, J. Electrochem. Soc. 142 (1995) L6.
20. J.P. Zheng, P.J. Cyang, T.R. Jow, J. Electrochem. Soc. 142 (1995) 2699.
21. Q.L. Fang, D.A. Evans, S.L. Roberson, J.P. Zheng, J. Electrochem. Soc. 148 (2001) A833.
22. J.P. Zheng, C.K. Huang, J. New Mater. Electrochem. Sys. 5 (2002) 41.
23. J.P. Zheng, Electrochem. Solid-State Lett. 2 (1999) 359.

24. R. Fu, Z. Ma, J.P. Zheng, J. Phys. Chem. B 106 (2002) 3592.
25. J.P. Zheng, T.R. Jow, J. Power Sources 62 (1996) 155.
26. T.R. Jow, J.P. Zheng, J. Electrochem. Soc. 145 (1998) 49.
27. J.P. Zheng, Y. Xin, J. Power Sources 110 (2002) 86.
28. J.W. Long, K.E. Swinder, C.I. Merzbacher, D.R. Rolison, Langmuir 15 (1999) 780.
29. J.W. Long, K.E. Swinder, C.I. Merzbacher, D.R. Rolison, Langmuir 19 (2003) 2532.
30. J.W. Long, K.E. Ayers, D.R. Rolison, J. Electroanal. Chem. 522 (2002) 58.
31. W. Dmowski, T. Egami, K.E. Swinder-Lyons, C.T. Love, D.R. Rolison, J. Phys. Chem. B 106 (2002) 12677.
32. D.A. McKeown, P.L. Hagans, L.P.P. Carette, A.E. Russell, K.E. Swinder, D.R.J. Rolison, Phys. Chem. B 103 (1999) 4825.
33. M. Vukovic, D.J. Cukman, Electroanal. Chem. 474 (1999) 167.
34. C.-C. Hu, Y.-H. Huang, J. Electrochem. Soc. 146 (1999) 2465.
35. I.-H. Kim, K.-B. Kim, Electrochem. Solid-State Lett. 4 (2001) A62.
36. W. Sugimoto, H. Iwata, Y. Yasunaga, Y. Murakami, Y. Takasu, Angew. Chem. Int. Ed. 42 (2003) 4092.
37. W. Sugimoto, M. Omoto, K. Yokoshima, Y. Murakami, Y. Takasu, J. Solid State Chem. 177 (2004) 4542.
38. W. Sugimoto, H. Iwata, Y. Murakami, Y. Takasu, J. Electrochem. Soc. 151 (2004) A1181.
39. W. Sugimoto, H. Iwata, K. Yokoshima, Y. Murakami, Y. Takasu, J. Phys. Chem. B 109 (2005) 7330.
40. Y. Takasu, C. Matsuo, T. Ohnuma, M. Ueno, Y. Murakami, Chem. Lett. 1998 (1998) 1235.
41. W. Sugimoto, T. Kizaki, K. Yokoshima, Y. Murakami, Y. Takasu, Electrochim. Acta 49 (2004) 313.
42. W. Sugimoto, T. Shibutani, Y. Murakami, Y. Takasu, Electrochem. Solid-State Lett. 5, (2002) A170.
43. Y. Takasu, X.-G. Zhang, Current Topics Electrochem. 5, (1997) 93.
44. S. Lavine, A.L. Smith, Discuss. Faraday Soc. 128 (1981) 2141.
45. P. Siviglia, A. Daghetti, S. Trasatti, Colloids and Surfaces 7 (1983) 15.

46. C. Chabanier, E. Irissou, D. Guay, J.F. Pelletier, M. Sutton, L.B. Lurio, Electrochem. Solid-State Lett. 5 (2002) E40.

Table 1. Selected parameters obtained by fitting the impedance data to the equivalent circuit (Fig. 6 inset) for anhydrous RuO_2, $RuO_2{\cdot}xH_2O$ and layered $H_{0.2}RuO_{2.1}{\cdot}nH_2O$.

Potential / V vs. RHE	C / F (g-RuO_2)$^{-1}$	T_{CPE} / F (g-RuO_2)$^{-1}$	$f_{\phi=-45}$ / Hz	f_{knee} / kHz	T_W / ms
RuO_2					
0.2	0.33(5)	14(2)	79.4	1.6	3.5(8)
0.4	0.33(3)	5.2(6)	158.5	2.5	1.7(2)
0.6	0.43(2)	9.6(4)	63.1	1.6	4.3(2)
0.8	0.290(7)	5.8(7)	63.1	2.0	4.0(2)
1.0	0.222(5)	6.2(3)	63.1	2.5	3.7(1)
1.2	0.233(7)	4(4)	50.0	2.5	4.8(7)
$RuO_2{\cdot}0.5H_2O$					
0.2	0.36(4)	150(40)	4.0	2.0	11(1)
0.4	0.41(2)	60(40)	4.0	1.6	77(8)
0.6	0.59(3)	80(40)	3.2	0.5	130(10)
0.8	0.43(3)	180(20)	2.5	1.2	33(2)
1.0	0.28(3)	170(20)	2.0	2.5	47(3)
1.2	0.25(4)	180(20)	2.0	3.2	52(3)
$H_{0.2}RuO_{2.1}{\cdot}nH_2O$					
0.2	0.36(1)	90(30)	5.0	0.5	14.0(9)
0.4	0.42(1)	130(30)	4.0	0.4	10.4(5)
0.6	0.54(2)	290(80	2.0	0.3	12(1)
0.8	0.30(1)	210(40)	3.2	0.6	5.2(4)
1.0	0.228(7)	160(20)	4.0	0.8	4.2(2)
1.2	0.236(6)	180(30)	3.2	0.6	4.3(3)

Figure Legends

Figure 1. The relation between gravimetric capacitance and the RuO_2 loading evaluated by the model electrode method. (Electrolyte: 1 M KOH (25ºC); v=50 mV s^{-1}; E= 0.3-1.1 V vs.RHE) [40].

Figure 2. Calculated specific capacitance and the specific surface area as a function of the particle size of RuO_2.

Figure 3. Cyclic voltammograms of RuO_2 thin film electrode at various scan rates. (Electrolyte: 0.5 M H_2SO_4 (25ºC); amount of RuO_2: 40 μg) [41].

Figure 4. The contribution of the specific capacitance at various scan rates [41].

Figure 5. Cyclic voltammograms of $RuO_2 \cdot 0.5H_2O$ thin film electrode at various scan rates. (Electrolyte: 0.5 M H_2SO_4 (25ºC); amount of active material: 40 μg) [39].

Figure 6. Frequency dependence of the phase angle for (a) $RuO_2 \cdot 0.5H_2O$ and (b) anhydrous RuO_2. The capacitor response frequency is shown with left arrows and the characteristic knee frequency is shown with bottom arrows. (Electrolyte: 0.5 M H_2SO_4 (25ºC); amount of active material: 40 μg). The equivalent circuit used for fitting the impedance data is shown in the inset [39].

Figure 7. (a) Cyclic voltammograms of layered $H_{0.2}RuO_{2.1} \cdot nH_2O$ thin film electrodes at various scan rates (Electrolyte: 0.5 M H_2SO_4 (25ºC); amount of active material: 40 μg). (b) Cyclic voltammograms of re-stacked ruthenium oxide nanosheet electrodes at various scan rates. (Electrolyte: 0.5 M H_2SO_4 (25ºC); amount of active material 3.6 μg-RuO_2) [36].

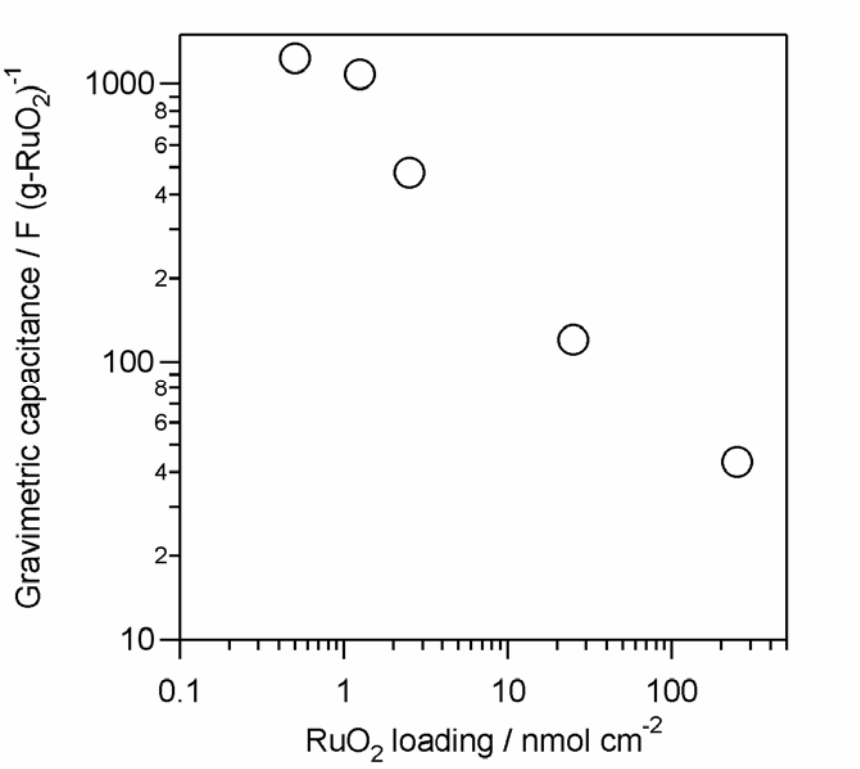
Gravimetric capacitance / F (g-RuO2)-1
1000
8
6
4
2
100
8
6
4
2
10
0.1
1
10
100
RuO2 loading / nmol cm-2

Figure 1.

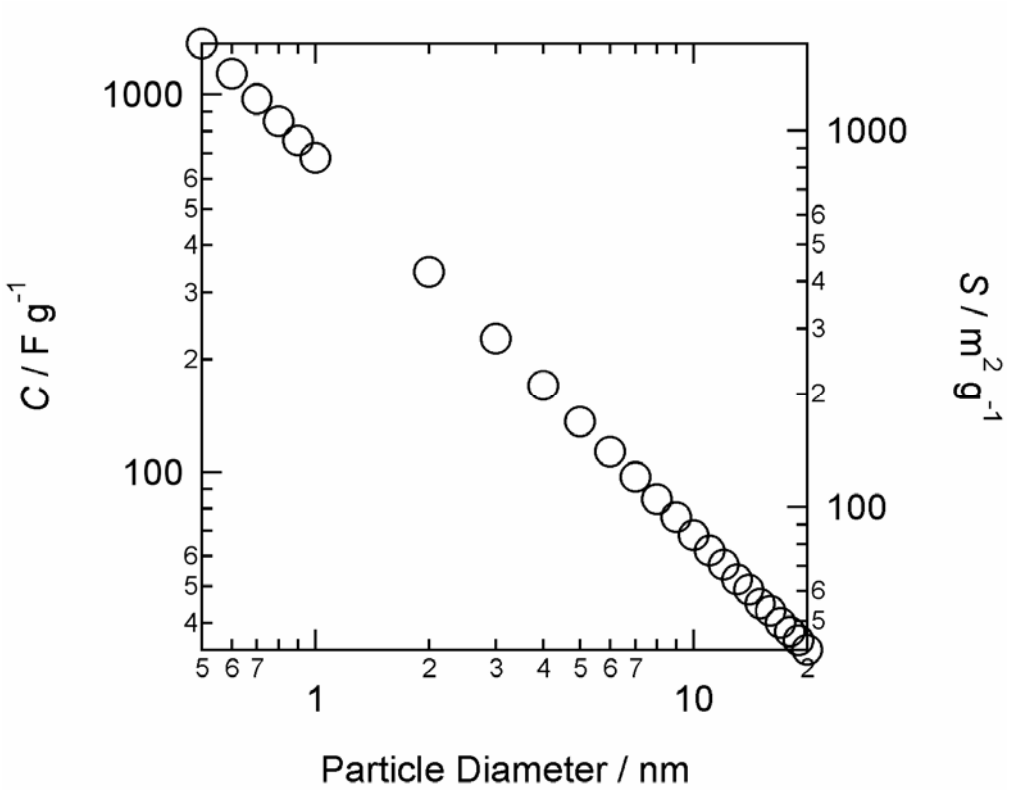

Figure 2.

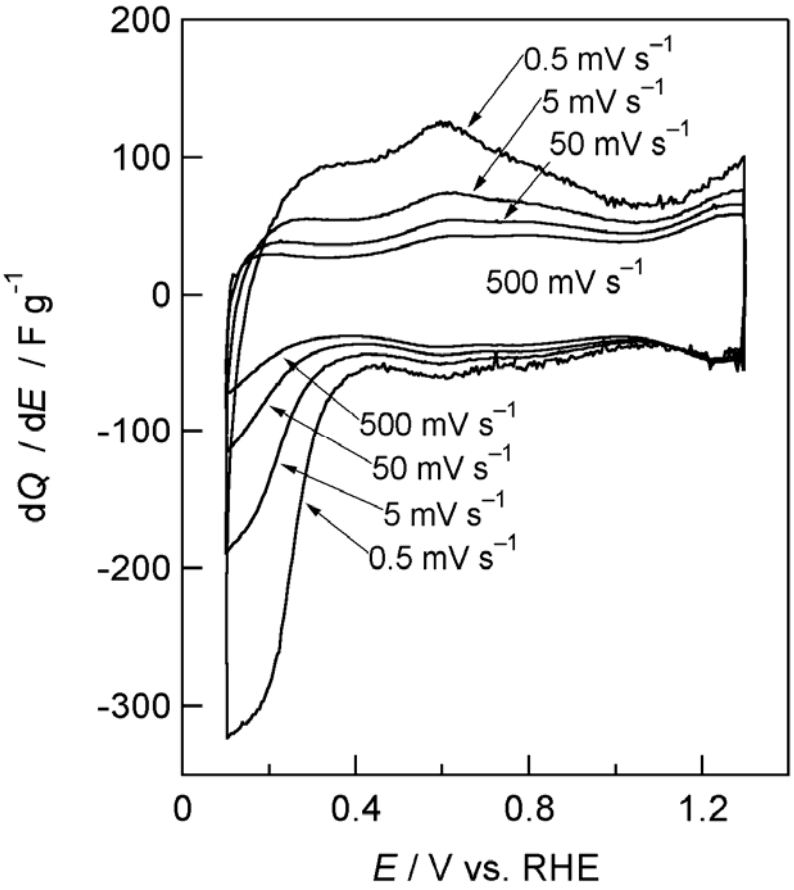
200
100
0
-100
-200
-300
0
0.4
0.8
1.2
dQ / dE / F g-1
E / V vs. RHE
0.5 mV s−1
5 mV s−1
50 mV s−1
500 mV s−1
500 mV s−1
50 mV s−1
5 mV s−1
0.5 mV s−1

Figure 3.

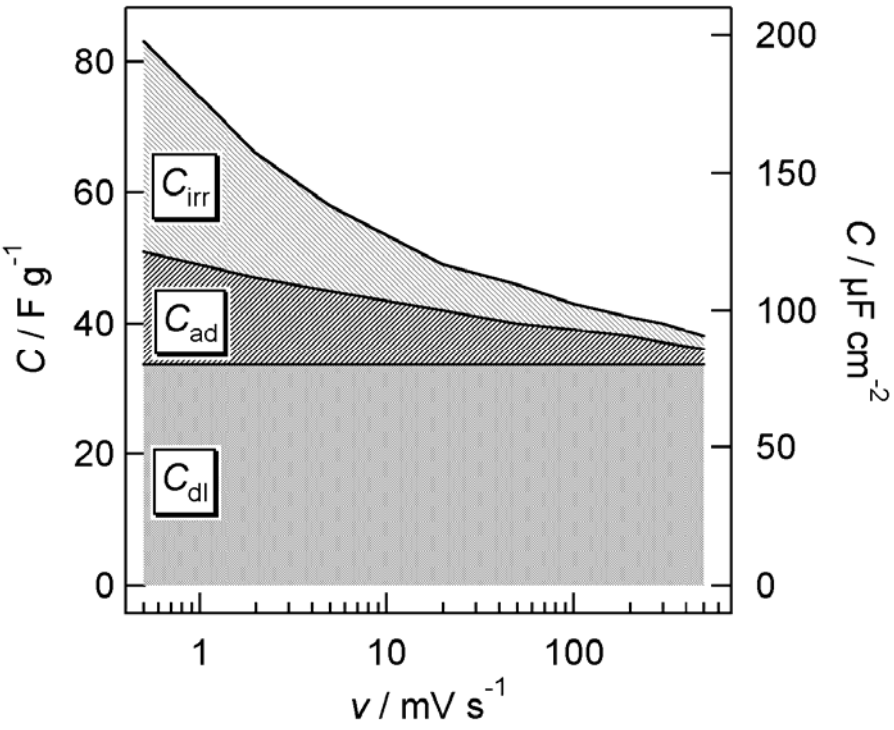
80
60
40
20
0
200
150
100
50
0
1
10
100
C / F g-1
C / μF cm-2
v / mV s-1
Cirr
Cad
Cdl

Figure 4.

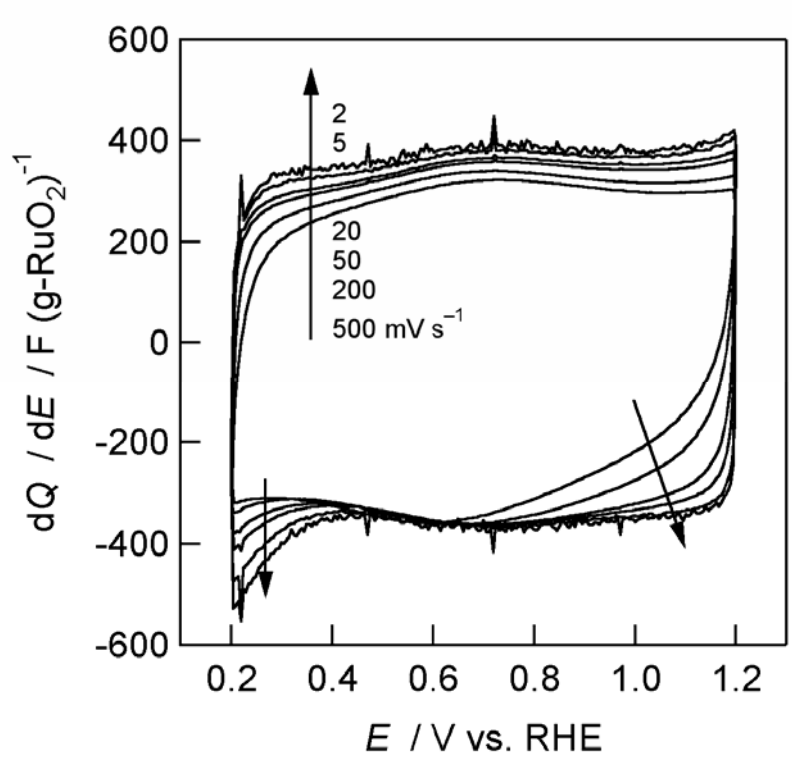
600
400
200
0
-200
-400
-600
0.2
0.4
0.6
0.8
1.0
1.2
dQ / dE / F (g-RuO2)-1
E / V vs. RHE
2
5
20
50
200
500 mV s-1

Figure 5.

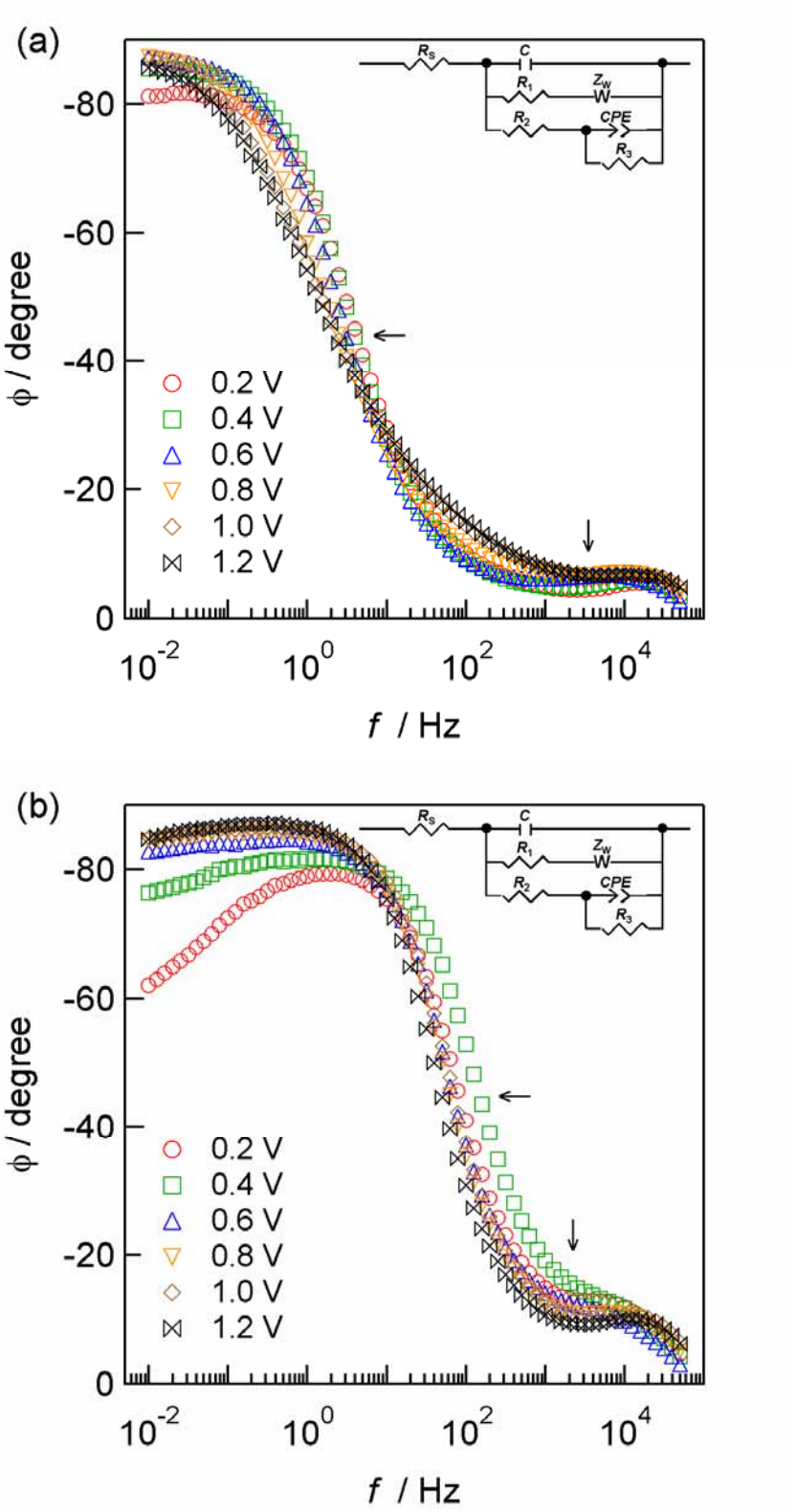
(a)
-80
-60
-40
-20
0
ϕ / degree
0.2 V
0.4 V
0.6 V
0.8 V
1.0 V
1.2 V
10^{-2}
10^{0}
10^{2}
10^{4}
f / Hz
R_S
C
R_1
Z_W
W
R_2
CPE
R_3
(b)
-80
-60
-40
-20
0
ϕ / degree
0.2 V
0.4 V
0.6 V
0.8 V
1.0 V
1.2 V
10^{-2}
10^{0}
10^{2}
10^{4}
f / Hz
R_S
C
R_1
Z_W
W
R_2
CPE
R_3

Figure 6.

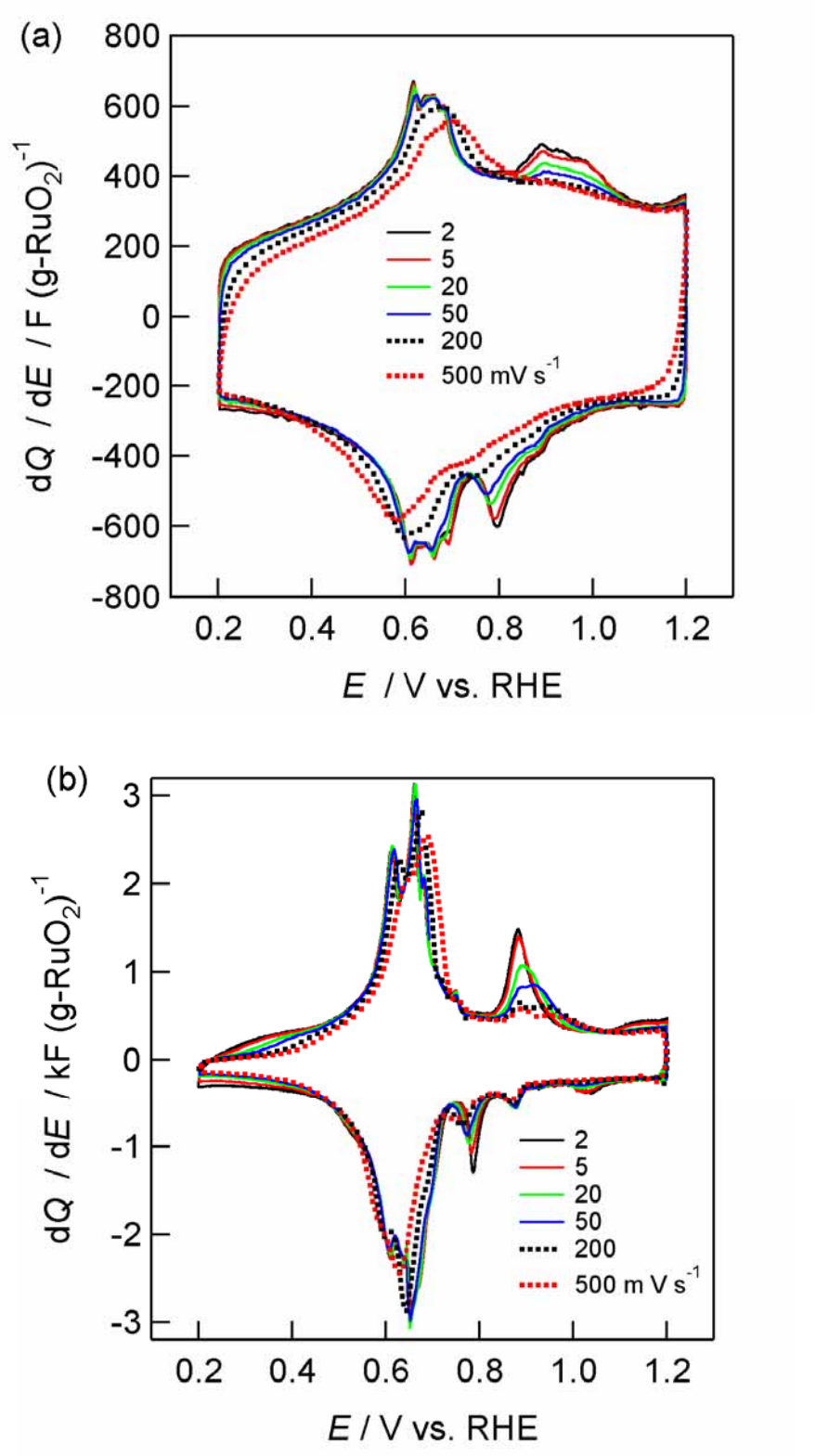
(a)
800
600
400
200
0
-200
-400
-600
-800
dQ / dE / F (g-RuO2)-1
2
5
20
50
200
500 mV s-1
0.2
0.4
0.6
0.8
1.0
1.2
E / V vs. RHE
(b)
3
2
1
0
-1
-2
-3
dQ / dE / kF (g-RuO2)-1
2
5
20
50
200
500 m V s-1
0.2
0.4
0.6
0.8
1.0
1.2
E / V vs. RHE

Figure 7.